Chapter 3

Evolution of CB-like microstructure in spinel systems by interpenetrating twins

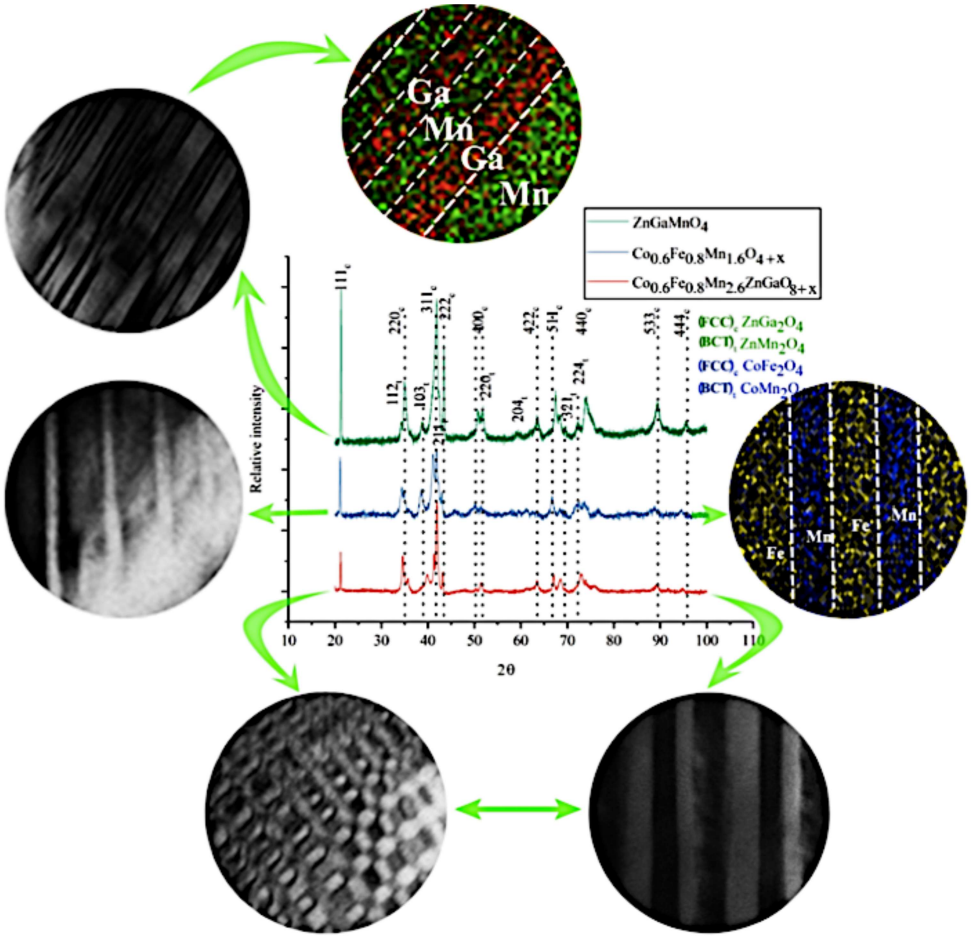

3.1 Introduction

Multicomponent high entropy metallic alloys have emerged over the last two decades as materials of both fundamental scientific interest and technological promise [1–4]. A number of possible areas of application ranging from structural applications to alternative energy and electronics have been identified for this class of alloys. However, the phase and microstructural stability of these alloys, any consequential changes in properties while in service, and service lifetime predictions for these alloys are still all active areas of research. By comparison, high entropy oxides are a more recent innovation; these too have their scientific challenges and technological opportunities [5]. Their electronic and electro-chemical properties are also promising. A clear understanding of their microstructure and properties at the atomic scale is also an area of active research.

Initially, high entropy metallic alloys were defined as single-phase solid solutions or intermetallic-based alloys. However, the number of metallic alloy systems with a single solid solution phase is limited [6], and instead many such alloys have been found to be multiphase. In addition, time and temperature-dependent composition changes have been observed in multicomponent high or medium entropy metallic alloys [7]. Therefore, the scientific community is now more inclined to term these materials as multicomponent alloys (MCAs) or complex concentrated alloys [8]. In the case of high entropy oxides, single phase materials have been observed upon quenching. However, so-called 'high entropy oxides' also tend to form multiple phases upon ageing, and so such materials are better regarded as multicomponent oxides (MCOs). MCOs are potential candidate materials for high-density memory devices, nanoscale batteries and thermo-electric devices [9,10]. Although microstructural design and stability has been discussed extensively in the MCA literature [11,12], there is much less discussion of these topics in the MCO literature [13,14]. MCOs in which the cation sublattice is occupied with multiple cations have been reported in a number of crystal structures such as rock salt, fluorite, perovskite and spinel [5,15]. Recently, both single and multiple oxide phase formation have been reported in MCOs [16,17]. However, the morphology of these phases, their distribution, the evolution of the final microstructure and the stability of the microstructure are all far from being completely understood.

In this chapter, the structural aspect of self-assembled and functionally different chessboard nanostructures has been explored. Our prime motive is to establish the correlation between crystal system and evolution mechanism. Since a critical review of early literature on CB-like microstructural evolution suggests that the evolution mechanism is crystal structure dependent,

in the present work, the author has explored CB-like evolution in spinel manganites, i.e., CoFeMn, ZnGaMn and CoFeGaMnZn to understand whether the evolution mechanism is similar for all these spinel manganites or there is some role of composition selection also. These chessboard nanostructures may find applications in high density memory storage, thermoelectric devices and in energy storage devices. CoFeMn and ZnGaMn oxides have been reported elsewhere to form self-assembled chessboard nanostructures from $CoFe_2O_4$ and $CoMn_2O_4$ spinels, and $ZnGa_2O_4$ and $ZnMn_2O_4$ spinels, respectively, after suitable heat treatment because of the diffusive separation of the ions into two different spinel phases [18–20]. In CoFeMn oxide, the two spinel domains are ferromagnetic and paramagnetic respectively. In ZnGaMn oxide, the two phases are thermoelectric and non-thermoelectric. In this chapter, the microstructural evolution in a CoFeGaMnZn MCO has been studied, and a comparison has been made with the microstructural evolution of the ternary CoFeMn and ZnGaMn oxides prepared in a similar manner. The main motive of this chapter is to establish the structural dependency of the evolution mechanism. For that purpose, spinel is taken as the system of interest.

3.2 Materials and methods

Self-assembled chessboard (CB) nanostructures in mixed CoFeMn, ZnGaMn and CoFeGaMnZn oxides were produced through a solid-state synthesis route chosen for ease of materials handling, its cost effectiveness, and its probability of success in producing pure end products. Ultra-high pure precursor powders of Co_3O_4, ZnO, Mn_2O_3, Ga_2O_3 and Fe_2O_3, each more than 99.99% purity (Sigma Aldrich & Alfa Aesar) were mixed and pelletized in stoichiometric proportions to obtain mixed oxides with compositions of $Co_{0.6}Fe_{0.8}Mn_{1.6}O_{4+\delta}$ ($\delta<<1$), $ZnGaMnO_4$ and $Co_{0.6}Fe_{0.8}GaMn_{2.6}ZnO_{8+\delta}$ ($\delta<<1$). In these stoichiometric calculations the oxidation states of Fe, Mn and Ga have been taken to be +3, while the oxidation states for Zn and Co have been taken to be +2. However, the oxidation states of the transition metals Co, Fe, Mn and Zn can vary, and this will clearly affect the defect chemistry and oxygen non-stoichiometry of the final phases. By contrast, the oxidation state of Ga can be taken to be +3 in both the oxide and in the spinel phases produced.

All the green pellets were sintered in air at 1250 °C for 24 hours followed by quenching into ice water. This heat treatment temperature and time was chosen to enable pellet densification and encourage diffusion of the various transition metal ions. To try and

encourage further more local, diffusive rearrangement of the cations below the phase transition temperatures of the constituent spinel phases, ageing treatments for all three mixed oxides were undertaken in air at 375 °C for 150 hours. Phase identification was undertaken by X-ray diffraction (XRD) in a Panalytical Empyrean high-resolution X-ray diffractometer operated at 40 kV with 40 mA current. For X-ray diffraction experiments Co-K_α radiation with wavelength of 1.78 Å was used. For transmission electron microscopy (TEM) observations, slices were obtained from both the periphery and the centre of the sintered and aged pellets and then ground separately into powder. For each TEM sample, the powder was suspended in ethanol and was subjected to ultrasonication for about 20 minutes before it was drop cast onto a carbon coated copper grid. TEM observations were made at 200 kV in a Tecnai G^2 T20 transmission electron microscope. Compositional mapping of the heat-treated oxide samples was obtained by scanning transmission electron microscopy (STEM) and X-ray energy dispersive spectroscopy (XEDS).

3.3 Results and discussion

3.3.1 X-ray diffraction analysis

Powder XRD patterns from the sintered and aged pellets of CoFeMn, ZnGaMn and CoFeGaMnZn oxides are shown in Figure 3.1. The pattern from CoFeMn oxide can be indexed

in terms of two spinel phases: $CoFe_2O_4$ (JCPDS card No. 00-022-1086) (space group $Fd\bar{3}m$ with $a \approx 8.3$ Å [18]) and $CoMn_2O_4$ (JCPDS card no. 00-001-1126) ($I4_1/amd$ with $a = 5.72$ Å and $c = 9.27$ Å), which have the cubic inverse spinel structure with a cubic F (FCC: Face centred cubic) Bravais lattice and a tetragonal I (BCT: Body centred tetragonal) spinel structure, respectively [21]. This indexing is not unique because there is a possibility that the phase(s) in the CoFeMn oxide pellet have mixed chemistries, altering subtly the nature of the phases present and their lattice parameters [19]. Similarly, the ZnGaMn oxide powder after sintering and ageing can be indexed in terms of two spinel phases: $ZnGa_2O_4$ (JCPDS card no. 00-038-1240) ($Fd\bar{3}m$ with $a = 8.33$ Å [19]) and $ZnMn_2O_4$ (JCPDS card no. 00-024-1133) ($I4_1/amd$ with $a = 5.66$ Å and $c = 9.34$ Å [21]), also with crystal structures with cubic F and tetragonal I Bravais lattices respectively. Here too, the indexing is not unique because of the

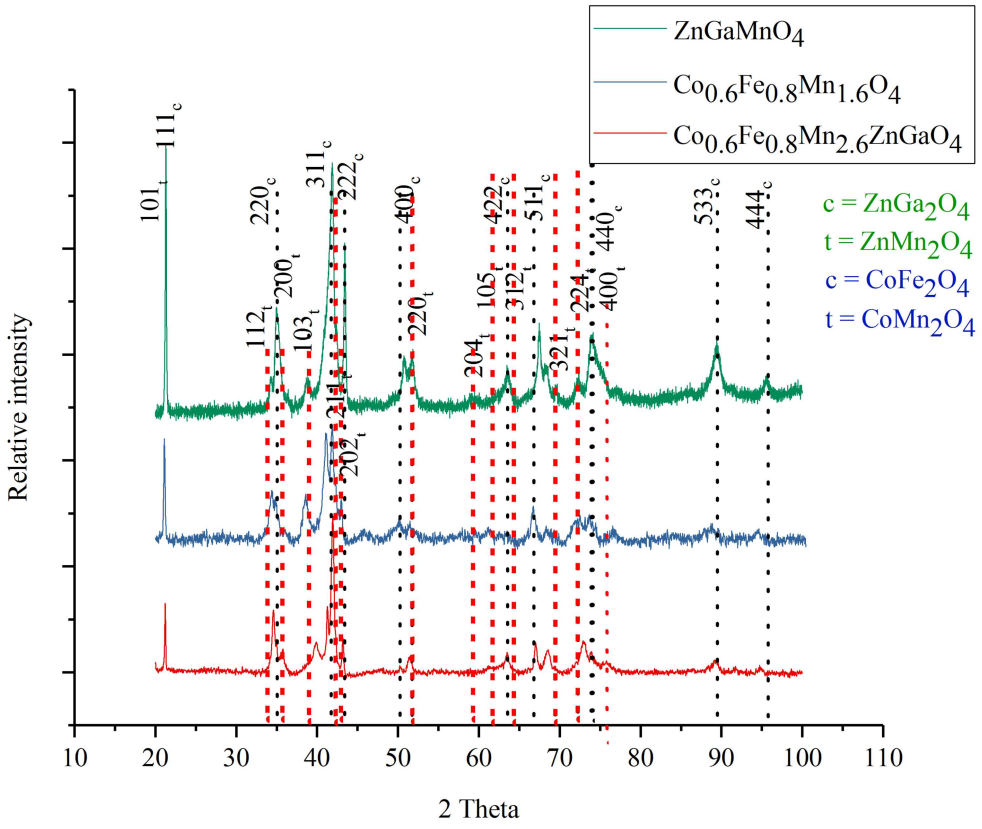

Figure 3.1: *Multiple display of powder XRD patterns of $ZnGaMnO_4$, $Co_{0.6}Fe_{0.8}Mn_{1.6}O_{4+\delta}$ ($\delta << 1$) and $Co_{0.6}Fe_{0.8}GaMn_{2.6}ZnO_{8+\delta}$ ($\delta << 1$) after sintering at 1250 °C for 24 hours followed by ageing at 375 °C for 150 hours. The XRD patterns indicate the presence of the cubic $Fd\bar{3}m$ $ZnGa_2O_4$ and tetragonal $I4_1/amd$ $ZnMn_2O_4$ phases in the pattern of $ZnGaMnO_4$, and the presence of the cubic $Fd\bar{3}m$ $CoFe_2O_4$ and tetragonal $I4_1/amd$ $CoMn_2O_4$ phases in the $Co_{0.6}Fe_{0.8}Mn_{1.6}O_{4+\delta}$ pattern. The cubic spinel peaks are marked with black dotted lines with reference to cubic $CoFe_2O_4$ and the tetragonal spinel peaks are marked with red dotted lines with reference to tetragonal $CoMn_2O_4$. These two patterns have been indexed with respect to the conventional unit cell descriptions for the two tetragonal phases. The XRD pattern of $Co_{0.6}Fe_{0.8}GaMn_{1.6}ZnO_{8+\delta}$ also shows signs of separation of similar cubic and tetragonal phases. Shifting in the $(103)_t$ and $(224)_t$ peaks of the tetragonal phase in the XRD pattern of $Co_{0.6}Fe_{0.8}GaMn_{1.6}ZnO_{8+\delta}$ with respect to $ZnMn_2O_4$ and $CoMn_2O_4$ is indicative of slight changes in the a and c lattice parameter.*

possibility that the mixed chemistries within the pellet changes the nature of the phase(s) present and their lattice parameters [20]. The quinary CoFeGaMnZn oxide also produces

an XRD pattern similar to those from CoFeMn oxide and ZnGaMn oxide. The diffraction peaks match quite closely those attributed to $CoFe_2O_4$, $CoMn_2O_4$, $ZnMn_2O_4$ and $ZnGa_2O_4$. The crystal structures of transition element-based spinel phases are sensitive to the cationic ratio, heat treatment temperature and cooling rate. In the case of manganate spinels, those with high manganese content tend to form tetragonal phases, while those with low manganese content tend to form cubic spinel phases at room temperature. Heat treatment temperatures and cooling rates also alters the cationic distribution in the interstitial sites that in turn can change the crystal symmetry [21]. However, the X-ray diffraction peaks are often quite broad, apart from the 111 and 222 peaks. This broadening of the peaks suggests that the microstructure is on a fine scale and that there may be a number of spinel phases present. The possibility of strain as an origin of the peak broadening is unlikely because the pellets were aged for a significantly long period of time. Some spinel peaks in the quinary oxide powder are shifted from the originally reported spinels: this might indicate the formation of novel mixed spinel phase(s) in the quinary oxide. In summary, it is evident that the X-ray diffraction information from the multicomponent oxide is difficult to deconvolute with confidence into individual spinel phases; this is why TEM is required in conjunction with X-ray diffraction for phase identification.

3.3.2 Diffraction contrast and Z-contrast imaging

Bright field images and corresponding electron diffraction patterns of the sintered and aged CoFeMn mixed oxide are shown in Figure 3.2. For these and the other TEM observations that we have made, it is convenient to use a tetragonal *F* (FCT) Bravais lattice description for the tetragonal structures observed, as others have also done [18,19], so that $a_{\text{f.c.t.}} = \sqrt{2}a_{\text{b.c.t.}} \approx 8 - 8.1$ Å, with a 45° rotation of the *x*-and *y*-axes highlighting the close structural relationship between the cubic FCC and tetragonal FCT forms of the spinels observed. The bright field image from the central region of the sintered and aged CoFeMn mixed oxide powder in Figure 3.2(a) has $\{022\}_{\text{FCT}}$ planes almost parallel to the electron beam. From the corresponding electron diffraction pattern along $[100]_{\text{FCT}}$ in (b), it is apparent that these $\{022\}_{\text{FCT}}$ planes are twin planes and that in (a) there are two sets of co-existing tetragonal domains twinned with

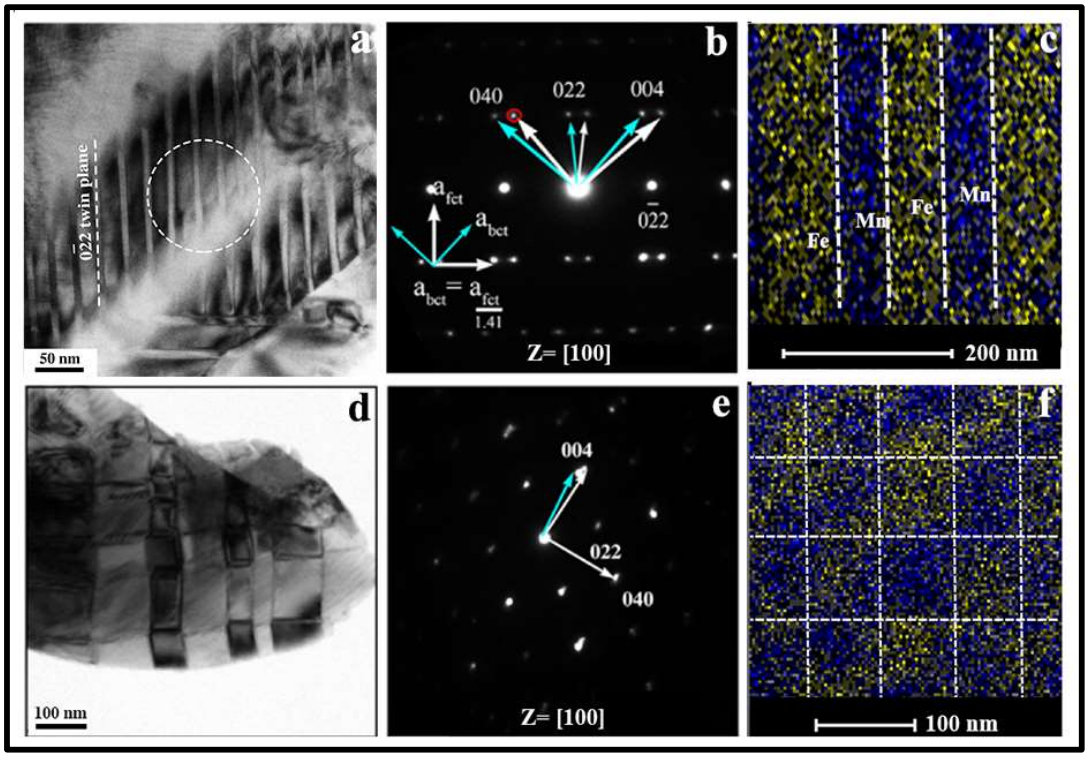

Figure 3.2: *(a) TEM diffraction contrast bright field image from the centre of the* $Co_{0.6}Fe_{0.8}Mn_{1.6}O_{4+\delta}$ *pellet sintered at 1250 °C for 24 hours followed by ageing at 375 °C for 150 hours showing two sets of co-existing tetragonal domains. Domain boundaries are parallel to* $(0\bar{2}2)$ *interface planes of the FCT unit cell. (b) Electron diffraction pattern from (a) showing twinning on the common* $(0\bar{2}2)$ *planes of the two domains. (c) HAADF-STEM-XEDS Z-contrast compositional mapping showing the segregation of Fe and Mn to alternating twinned regions. (d) Bright field image from the periphery of the* $Co_{0.6}Fe_{0.8}Mn_{1.6}O_{4+\delta}$ *pellet after sintering and ageing as described for (a) showing cuboidal nanodomains observed slightly off axis from a [100] zone. (e) Electron diffraction pattern from the region in (d) consistent with the presence of cubic and tetragonal phases. The interfaces of the squared nanodomains are along {022} family of planes with respect to the FCC and FCT unit cells of the cubic and tetragonal phase. (f) HAADF-STEM-XEDS Z-contrast compositional map from the cuboidal nanodomains showing the onset of separation of Fe and Mn in two neighbouring nanodomains.*

respect to one another by a 180° rotation about the normal to the plane whose reflection in Figure 3.2(b) is labelled as $0\bar{2}2$. Reflections in Figure 3.2(b) from one set of tetragonal domains are arrowed in white and reflections from the other set of domains are arrowed in

light blue. Had a tetragonal BCT unit cell description been used, these twinning planes would have been indexed as $\{112\}_{BCT}$ twins. While others have described such twinning planes in phases with tetragonal *I* lattices as $\{011\}_{FCT}$, such as in In–Tl martensite [22], we have chosen here to describe these twin planes as $\{022\}_{FCT}$ planes rather than $\{011\}_{FCT}$ planes because $\{011\}_{FCT}$ planes have fractional indices with respect to the conventional tetragonal *I* unit cell. High angle annular dark field-STEM (HAADF-STEM) Z-contrast compositional mapping (XEDS) of these twinned regions is shown in Figure 3.2(c). This shows evidence of segregation of Fe and Mn to alternating twinned regions. This segregation can be rationalized in terms of the pseudo-spinodal decomposition model described by Ni and Khachaturyan [20]. However, here, this is with respect to decomposition within a twinned tetragonal FCT spinel phase where there would seem to be no changes in lattice parameter between the twinned regions as a consequence of the chemical ordering. This composition map represents a different projection view of the sample, as the sample is tilted by ~19° with respect to the bright field image in Figure 3.2(a) towards the detector while collecting the composition map. In addition, it is worth noting that the width of the twinned domains in Figure 3.2(a) is ~30 nm, while the width of the compositionally separated domains in Figure 3.2(c) is ~70 nm. Furthermore, as we have noted, the composition separation might well be incomplete, and this might result in incommensurate observations of widths between the twinned domains and compositionally separated domains. STEM-HAADF-EDS map of the similar twinned region with no tilt is shown in Figure 3.3 (b-f). It is apparent in Figure 3.3(a) that the twinned regions are ~70 nm wide and the compositionally separated Fe and Mn domains (Figures 3.3(b) and 3.3(c), respectively) are also ~70 nm wide. These differing width observations can be attributed both to the tilting of the specimen and also to the incompleteness of the composition separation process. In addition, it is observed that oxygen and cobalt (Figures 3.3(e) and 3.3(f), respectively) are uniformly distributed in the sample. Nano-beam electron diffraction patterns obtained from the white spot in Figure 3.3(a), such as that given in Figure 3.3(d) indicates that the spinel phase that forms is a tetragonal phase.

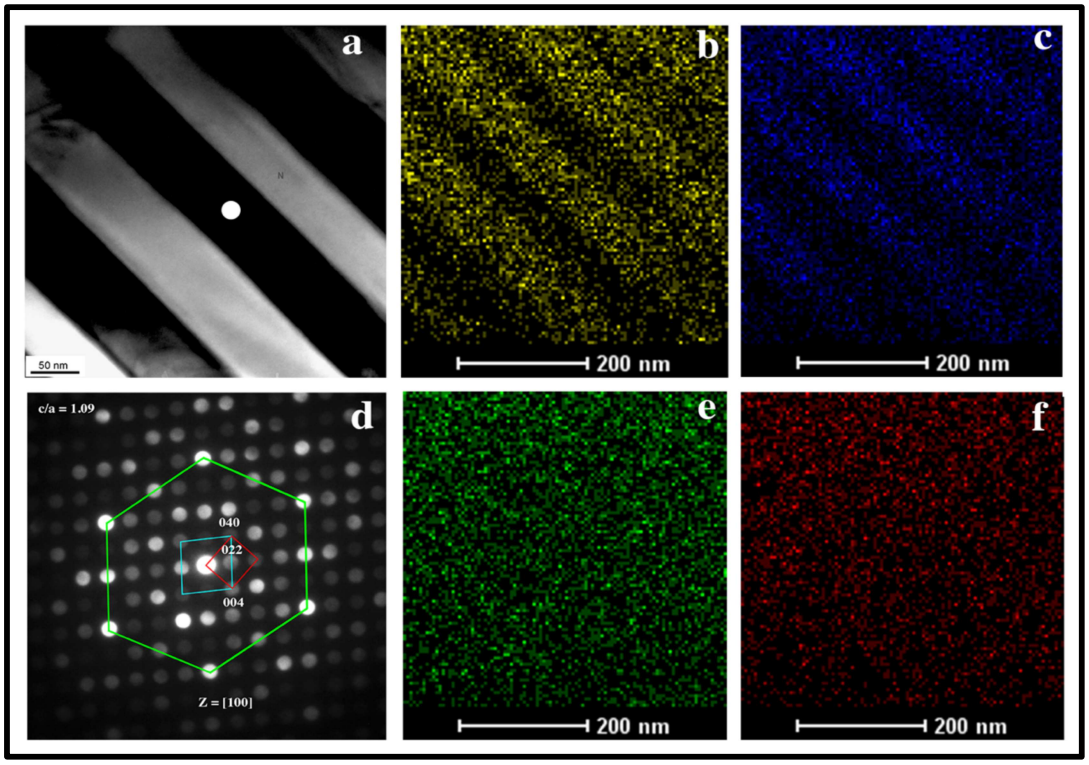

Figure 3.3: *(a) Diffraction contrast image of the* $Co_{0.6}Fe_{0.8}Mn_{1.6}O_{4+\delta}$ *(*$\delta << 1$*) after heat treatment at 1250 °C for 24 hours followed by quenching in ice water. Subsequently it was aged at 375 °C for 150 hours. In the diffraction contrast image alternate bands of Fe-rich and Mn-rich domains are observed. The width of the individual bands is ~70 nm. STEM-HAADF-EDS mapping is shown for (b) Fe, (c) Mn, (e) O and (f) Co. Co and O are uniformly distributed while Fe and Mn are alternately distributed in the bands. (d) Nano-beam electron diffraction pattern from the white point in the dark band in (a). In the diffraction pattern the tetragonal symmetry of the band is clearly observed.*

A bright field image and the corresponding electron diffraction pattern from the peripheral region of the pellet are shown in Figures 3.2(d) and 3.2(e), respectively. In the bright field image rectangular alternating bright and dark domains are observed, similar to chessboard (or checkerboard) regions seen in Mg-doped $CoFe_2O_4$ spinel by Zhang et al. [18] and interpreted by them in terms of coexisting cubic and tetragonal domains. The size of the domains in Figure 3.2(d) are ~80–100 nm and the boundaries between adjacent domains are nearly edge-on. The prominent electron diffraction pattern in Figure 3.2(e) can be indexed as $[100]_{FCT}$, so that, as is evident in the electron diffraction pattern, the 022 and $02\bar{2}$ systematic rows of reflections are not perpendicular to one another. The reflection

arrowed in blue has an interplanar spacing consistent with it being from the FCC cubic spinel phase.

The lattice parameters for the FCT tetragonal spinel phase calculated from the electron diffraction patterns are $a \approx 8.1$ Å and $c \approx 8.8$ Å, similar to the reported lattice parameters of $CoMn_2O_4$, but with a smaller '*c*'. This difference can be attributed to the existence of mixed chemistries in the tetragonal domains. The HAADF-STEM compositional map (XEDS) in Figure 3.2(f) from the region shown in Figure 3.2(d), shows that alternate domains are preferentially rich in Fe and Mn respectively. There is incomplete segregation of Fe and Mn within these nanodomains similar to observations made elsewhere by Zhang et al. [18]. To establish the correlation between the crystal structure and evolution mechanism, similar experiments were repeated on other spinel systems, i.e., $ZnGaMnO_4$ and $CoFeGaMnZnO_{8+\delta}$. Bright field images from the central and peripheral regions of the sintered and aged pellet of ZnGaMn oxide and the corresponding diffraction patterns and HAADF-STEM composition maps (XEDS) from the central region are shown in Figure 3.4. Twin plane is $\{022\}_{FCT}$. Here, the common zone axis can be labelled as $[31\bar{1}]$ and the twins can be labelled as $(022)_{FCT}$ planes. Other than the common 022 set of reflections, reflections in Figure 3.4(b) from one set of twins are highlighted in blue and reflections from the other set of twins are highlighted in red. The HAADF-STEM composition maps (XEDS) from the central region shown in Figures 3.4(c) and 3.4(f) show that there is preferential segregation within these twinned tetragonal regions of Mn and Ga, while the Zn composition is almost uniform. A diffraction contrast bright field image and STEM-HAADF-XEDS composition maps from a similar area of the $ZnGaMnO_4$ sample are given in Figures 3.5(b) and 3.5 (c-f), respectively. As with Figure 3.4(b), the electron diffraction pattern in Figure 3.4(b) can be interpreted straightforwardly in terms of twinned tetragonal regions present in Figure 3.4(a) where the similar banded contrast arising from the composition separation between Mn and Ga can be observed in the Z-contrast HAADF-STEM image in Figure 3.5(a). In the diffraction contrast bright field image (Figure 3.5(b)) similar bands arising from composition separation could also be observed. The width of the bands is ~70 nm. In the composition maps (Figures 3.5(d) and 3.5(e)), it is observed that Zn is homogeneously distributed, whereas Mn and Ga are distributed in alternate bands.

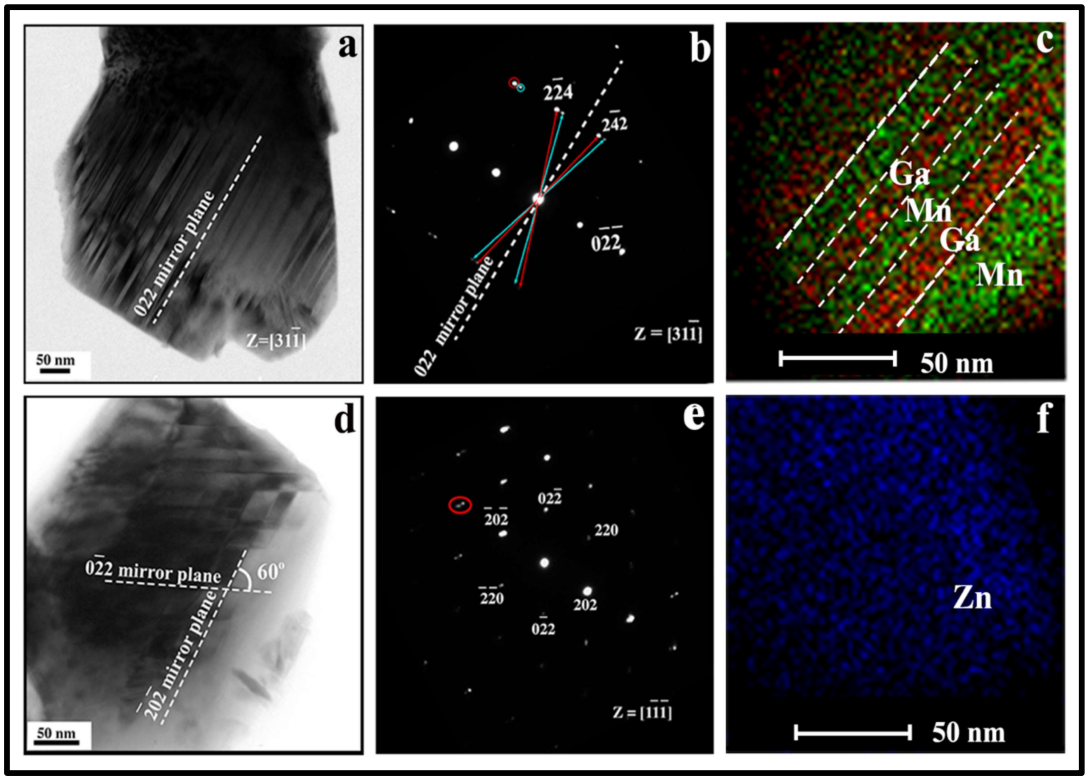

Figure 3.4: *(a) TEM bright field image from the centre of the $ZnGaMnO_4$ pellet after sintering at 1250 °C for 24 hours and subsequent ageing at 375 °C for 150 hours. A striped microstructure is apparent arising from the presence of two sets of domains. (b) Electron diffraction pattern from (a) indexed with respect to the doubly primitive FCT unit cell showing that twinning has occurred on* (022) *interface planes. (c) HAADF-STEM-XEDS Z-contrast compositional map showing the segregation of Ga and Mn to alternating twinned regions. (d) Bright field image from the periphery of the same pellet showing a chessboard-like morphology with* $(0\bar{2}2)$ *and* $(\bar{2}0\bar{2})$ *twin planes denoted by dotted lines. (e) Split in the {202} family of spots in the corresponding rotationally oriented diffraction pattern along the* $[1\,\bar{1}\,\bar{1}]$ *zone axis showing the twinned orientation relationship between the domains. (f) HAADF-STEM-XEDS Z-contrast compositional mapping of Zn in the region shown in (c). It is evident that the Zn is almost uniformly distributed within the two twinned regions.*

The composite composition map for Mn and Ga is given in Figure 3.5(c). As with the situation found in the centre of the CoFeMn oxide pellet, the lattice parameters in the twinned regions seem unchanged by the chemical ordering. A bright field image and the

corresponding rotationally aligned diffraction pattern from the peripheral region of the sintered and aged pellet are given in Figure 3.4(d) and Figure 3.4(e) respectively.

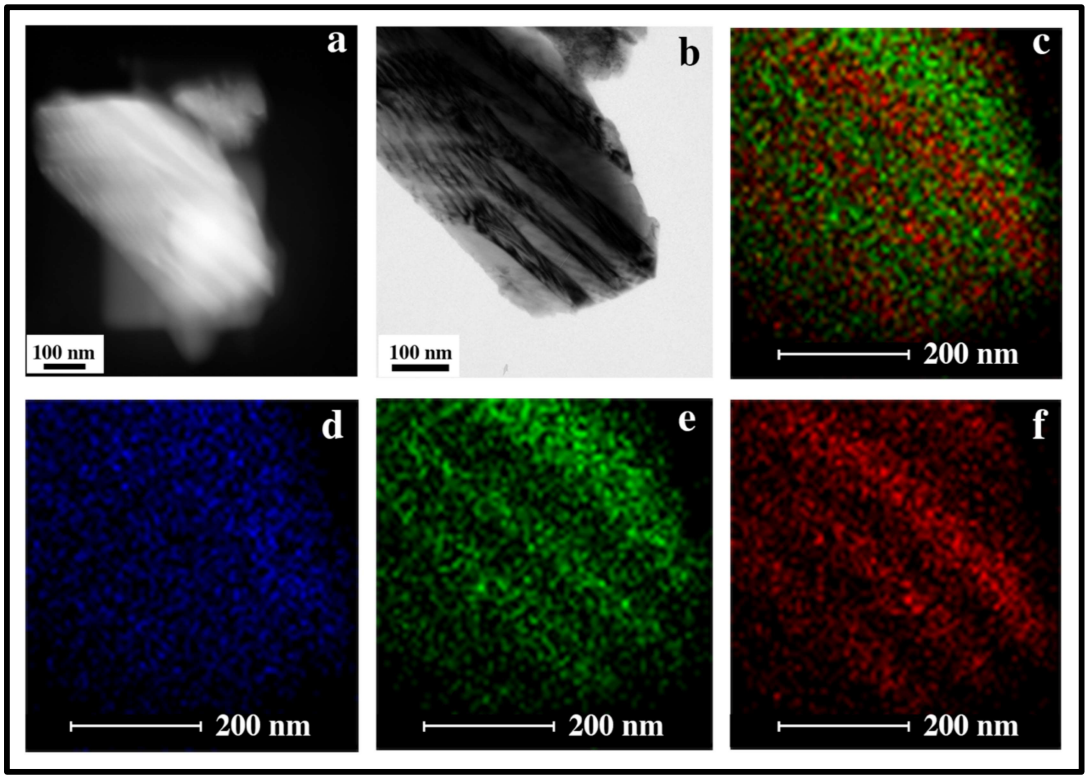

Figure 3.5: *(a) HAADF image (b) diffraction contrast bright field image of the $ZnGaMnO_4$ after heat treatment at 1250 ℃ for 24 hours followed by quenching in ice water. Subsequently this was aged at 375 ℃ for 150 hours. In the HAADF and the bright field image an alternate banded structure is observed. STEM-HAADF-EDS maps are shown for (c) Ga+Mn overlay (d) Zn (e) Mn and (f) Ga. The alternate bands of Mn and Ga rich domains are ~70 nm wide.*

In the bright field image chessboard-like contrast is observed, but the alternating bright and dark domains are not rectangular in appearance, but instead rhombus-like with an internal angle of ≈ 60°. The electron diffraction pattern shown in Figure 3.4(e) is consistent with the presence of only FCT tetragonal domains. The lattice parameters measured from Figure 3.4(e) are $a \approx 8.2$ Å and $c \approx 8.7$ Å. These match with those of $ZnMn_2O_4$ with a suitable change in chemical composition to modify the lattice parameters. The domain structure seen in Figure 3.4(d) is reminiscent of interpenetrating twin morphologies reported in the tetragonal *F* In–Tl phase with a $c/a \approx 1.04$ [23] and also in the tetragonal *I* Ni–Mn–Ga

phase which has an equivalent $c/a \approx 1.20$ when described in terms of a FCT tetragonal unit cell [24].

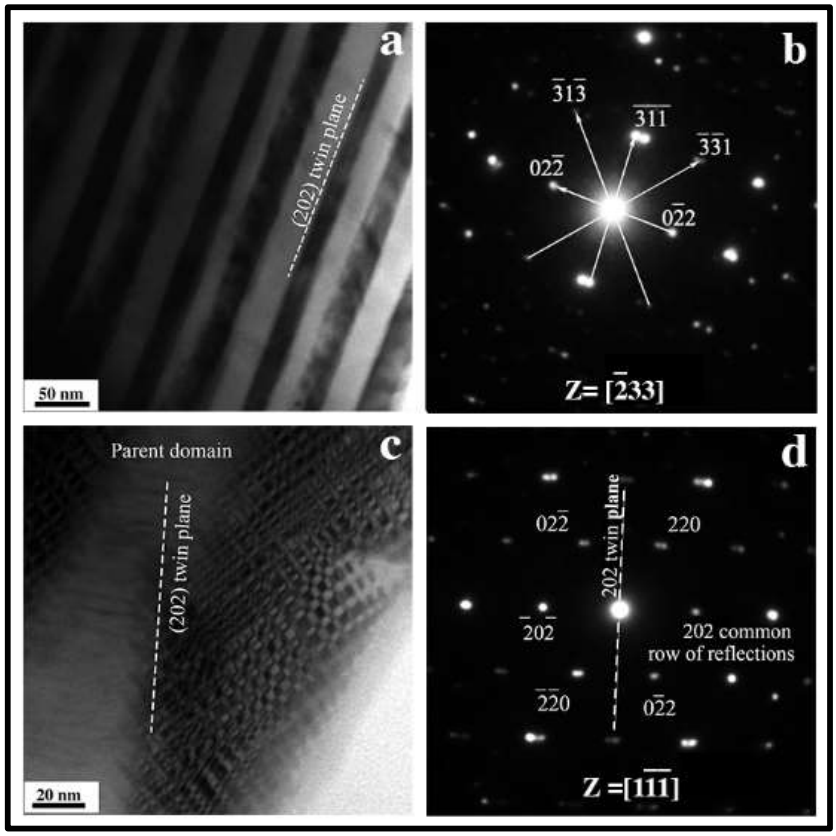

Figure 3.6: *(a) TEM bright field image from the centre of the* $Co_{0.6}Fe_{0.8}Mn_{1.6}ZnGaO_{8+\delta}$ *($\delta << 1$) pellet after sintering at 1250 °C for 24 hours and subsequent ageing at 375 °C for 150 hours. Twinned regions are evident. Each region is internally twinned on* $\{202\}_{FCT}$ *planes. (b) Electron diffraction pattern from (a) along a* $[\bar{2}33]$ *direction. (c) Bright field image from the periphery of the pellet showing a chessboard-like morphology, with alternating dark and bright nanodomains. (d) electron diffraction pattern from (c) indicating that within this chessboard-like morphology twinning has occurred on* $(202)_{FCT}$ *planes in (c).*

Bright field images and the corresponding electron diffraction patterns from the central and peripheral regions of the sintered and aged CoFeGaMnZn mixed oxide pellet are shown in Figure 3.6. In Figure 3.6(a) tetragonal *F* domains twinned on $\{022\}_{FCT}$ planes are visible, confirmed by the electron diffraction pattern in Figure 3.6(b). The peripheral region of the sintered and aged pellet seen in Figure 3.6(c) has a chessboard-like nanostructure with

alternative bright and dark contrast similar to that seen in Figure 3.2(d), but on a much finer scale than in Figure 2(d). The electron diffraction pattern from Figure 3.6(c) shown in Figure 3.6(d) suggests that, as in Figure 3.4(e), there are only tetragonal FCT domains present in Figure 3.6(c). A HAADF image and STEM-HAADF-XEDS composition maps from the central region of the sintered and aged CoFeGaMnZn mixed oxide are shown in Figure 3.7 (b-g). In the HAADF image linear contrast arising out of the twin formation is observed. However, in the composition maps, in contrast to the ternary oxides, no visible segregation of the chemical elements is observed. The area XEDS spectrum from the same sample is shown in Figure 3.8. In this spectrum, the presence of all the metallic elements, i.e. Co, Fe, Ga, Mn and Zn can be established. The composition after background correction is given at the side of the spectrum. This is consistent with the starting composition.

This MCO based on a five component CoFeGaMnZn oxide is a new observation, as is the chessboard microstructure in this system seen here in the periphery of the 150 hours aged pellet. While after 150 hours of ageing at 375 °C, the microstructure is dominated by a twinned tetragonal phase, in line with the relative intensities of the 112_t and 220_c diffraction peaks in Figure 3.1 from this five-component oxide, after far longer ageing times there is more of a 50:50 mixture of cubic and tetragonal spinel phases, as we will report in subsequent chapters. At this stage of ageing, composition separation is not significantly seen because no distinct separation of the elemental species is observed in the STEM-EDS composition maps for Co, Fe, Ga, Mn and Zn. This is consistent with the XRD pattern shown in Figure 3.1, where splitting of the diffraction peaks is not a prominent feature. However, the splitting of the major XRD peaks is visibly present in Figure 3.1 for the CoFeMn and ZnGaMn ternary oxides, for which compositional separation has progressed and the compositionally separated domains have also grown significantly after 150 hours of ageing at 375 °C.

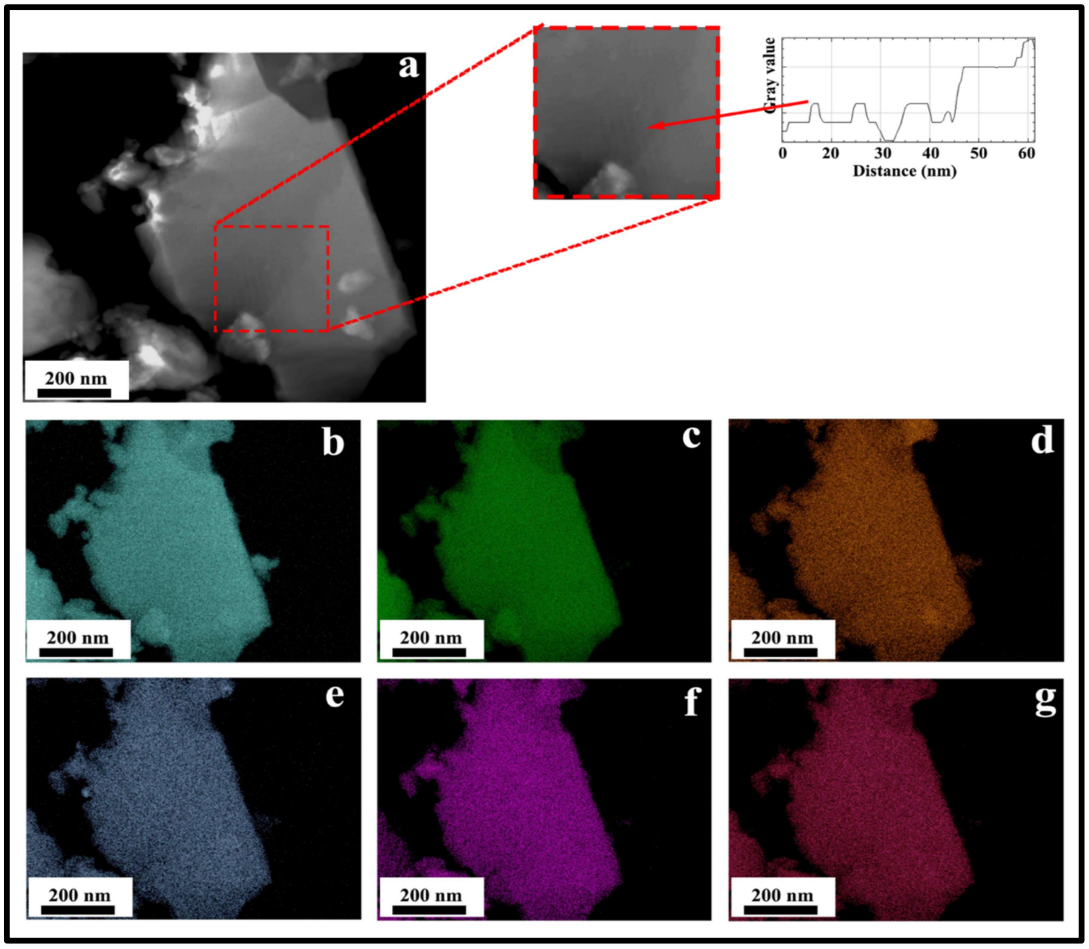

Figure 3.7: *STEM-HAADF-EDS mapping of the* $Co_{0.6}Fe_{0.8}GaMn_{2.6}ZnO_{8+\delta}$ *(*$\delta << 1$*) after heat treatment at 1250 °C for 24 hours followed by quenching in ice water. Subsequently this was aged at 375 °C for 150 hours. In the HAADF image in (a) very faint linear contrast corresponding to the twins can be observed. EDS maps corresponding to (b) O (c) Mn (d) Fe (e) Co (f) Ga and (g) Zn show uniform distribution, indicating that the MCO after this aging treatment does not undergo significant composition separation.*

A detailed study on composition separation within this five component CoFeGaMnZn oxide as it evolves over far longer hours of ageing will be discussed in subsequent chapters. The mechanism behind the evolution of the chessboard-like nanostructure in this five-component oxide would seem to be similar to that discussed in the literature for oxides with fewer components [18–20], with the additional consideration that very similar nanostructures can also be produced by interpenetrating twins of a single phase, with or without a pseudo-spinodal decomposition process.

The twinning seen in the tetragonal phase can be described in the formal theory of deformation twinning [25] as being either defined by $K_1 = (101), K_2 = (10\bar{1})$, $\eta_1 = (10\bar{1})$, $\eta_2 = [101]$, s = (c/a) – (a/c) using a tetragonal F lattice description [22] or by $K_1 = (112), K_2 = (11\bar{2})$, $\eta_1 = (11\bar{1})$, $\eta_2 = [111]$, $s = (\sqrt{2}\,c/a) - (a/\sqrt{2}\,c)$ using a tetragonal I lattice description [24], where K_1, K_2, η_1, η_2 and s have their usual meanings in deformation twinning crystallography [25]. In the mixed oxides it is reasonable to assume that the twinning seen in the tetragonal spinels is a consequence of the degree of strain energy within the crystal. The strain energy in the CoFeGaMnZn MCO is likely to be quite high because of the presence of several different ionic species in the lattice. In order to minimize the strain energy, the lattice twins. The formation of multiple interpenetrating twins with different variants leads to the evolution of a chessboard morphology, with or without a second cubic spinel phase. It is relevant that stacking faults were not seen in any of these oxide systems. As the tetragonal spinel structures twin and also exhibit pseudo-spinodal decomposition, the nanodomains are quite similar in terms of lattice parameters as a consequence. Furthermore, there was no evidence of extensive arrangements of dislocation networks at interfaces within the nanostructure. It could reasonably be expected that the long heat treatment time at elevated temperatures would help to minimize any interfacial strain through the annihilation of defects at interfaces. The chessboard nanodomains in the MCO are significantly smaller than those in the ternary oxides. We attribute this to the lower diffusivity of ionic species in the MCO, which makes it resistant to grain growth, and we note that this is consistent with the recent report of grain growth resistance in high entropy alloys [26]. Despite the fruitful information gathered by diffraction contrast and HAADF-STEM Z-contrast imaging, a detailed explanation of CB-like microstructural evolution cannot be made, especially the interfacial arrangement of the nanodomains and the orientation relationship of parental and product domains (subdomains). The phase-contrast imaging techniques can resolve this issue by providing atomistic data containing chemical and positioning information.

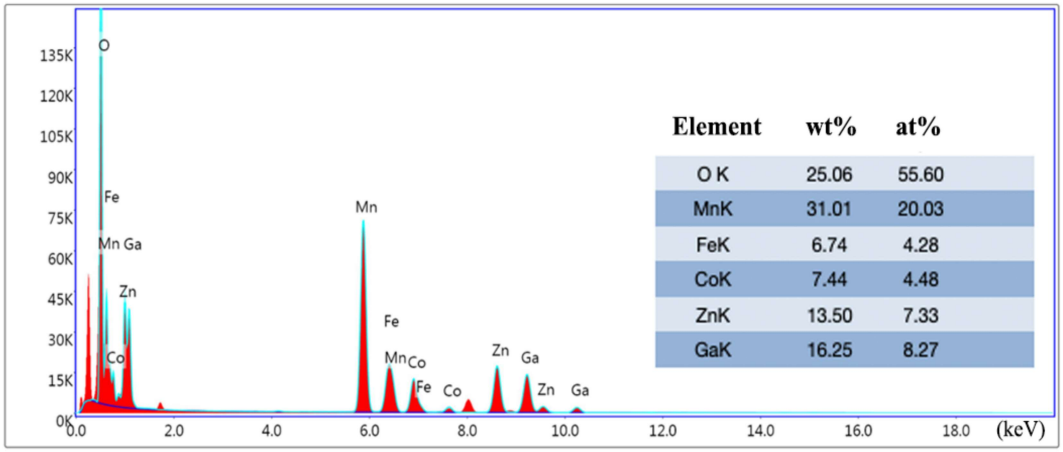

Figure 3.8: *XEDS spectrum of the* $Co_{0.6}Fe_{0.8}GaMn_{2.6}ZnO_{8+\delta}$ *(δ << 1) after heat treatment at 1250 °C for 24 hours followed by quenching in ice water. Subsequently this was aged at 375 °C for 150 hours. Compositions in wt% and in at% obtained after the background correction are given to the right of the spectrum. These are consistent with the starting composition, so that the relative ratios of different elements are also maintained.*

3.3.3 Phase contrast imaging

High-resolution (HR) phase contrast imaging coupled with multislice image simulation is used to complement the above-mentioned TEM techniques to characterize intricate details of CB-like nanostructures. Amongst all the microstructural features, interfacial atomic arrangement of nanodomains is the most informative feature to understand the morphology of the CB-like systems. To comprehend the nature of the interfaces and their atomic arrangements in manganite spinels based CB-like nanostructures, CoFeMnO spinel system was taken as a system of interest and was investigated with phase-contrast HR imaging. To this stage of the investigation, XRD and TEM analysis have established a settled difference in lattice parameters and chemistry of both the phases. The difference between the lattice parameters of cubic and tetragonal phases, misfit strain energy is introduced in the system. To neutralize this misfit strain energy, system initiates a mutual solid-body rotation between nanodomains. However, for the given CB system, maximum difference between the lattice parameters of two phase is (c_t - a_c) ~10%, which falls under coherent regime of the interfaces. A mutual rotation of two nanodomains rejects the possibility of formation of coherent interfaces in first sight (Figure 3.2-3.4) as the two neighboring domains have related crystal structure with minute difference in lattice parameters. The Phase contrast

HR images and corresponding FFTs (shown in the inset) collected at an interface of the cubic and tetragonal domain along [$\bar{1}12$] and [$\bar{1}11$] directions (Figures 3.9, and 3.10, respectively) depict their semi-coherent nature along {220}.

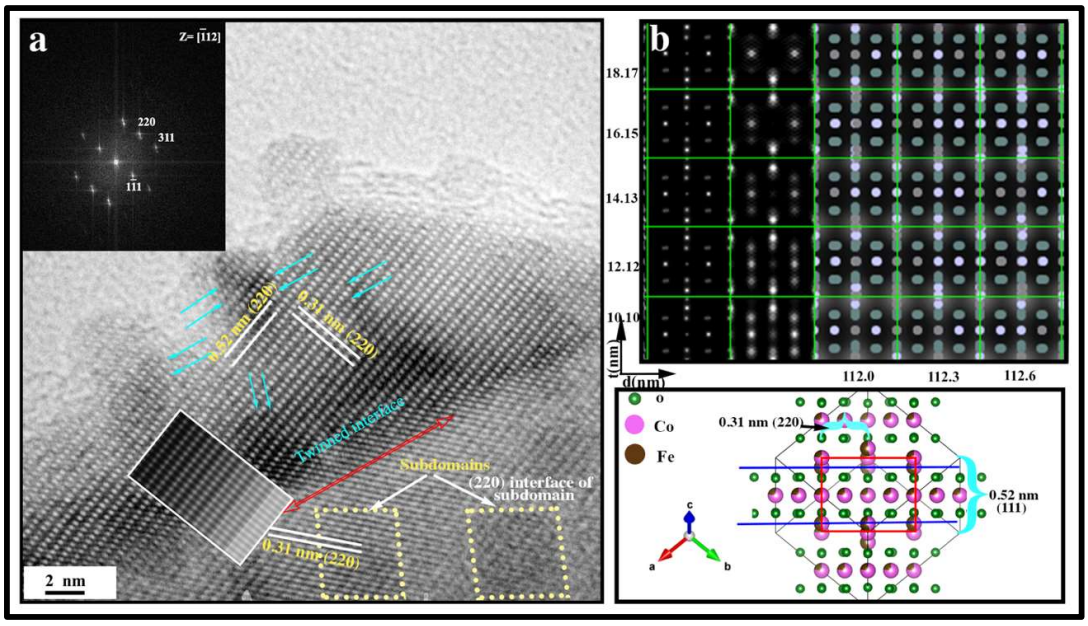

Figure 3.9: *(a) Phase contrast high-resolution image of* $Co_{0.6}Fe_{0.8}Mn_{1.6}O_{4+\delta}$ *(δ<<1) along* [$\bar{1}12$] *zone axis after heat treated at 1250 ℃ for 24 hours followed by quenching in ice water and after a subsequent aging at 375 ℃ for 150 hours. In the same image, simulated HR image is overlaid on experimental image (surrounded by solid white rectangle), whereas subdomains are marked with dotted yellow rhombus, and their presence can be visualized by the variation in contrast in the image (the interfaces are marked with cyan arrows), (b) corresponding defocus-thickness map generated by Multislice simulation method performed with voltage = 200kV,* C_s *= 1.2 mm and* Δf_{Sch} *= -65.83 nm. parameters used. (c) perspective view of unit cell of* $CoFe_2O_4$ *along* [$\bar{1}12$].

Semi coherency at the interface is evident by bend continuity of the {220} planes through both the phases (marked by red arrow in Figure 3.9 (a)). These two phases are expected to form interfaces along the planes with minimum d-spacings to minimize the misfit strain energies. In this case, the d-spacing is the smallest for {220} planes. Formation of the coherent interfaces between two neighboring domains only can be achieved, when the difference in d-spacing would be less than 10%. Moreover, the absence of interfacial

dislocation refers that the diffusional kinetics in evolution of CB-like nanostructure of spinel manganites through solid state synthesis route does not involve vacancies to diffuse the atoms from one phase to another. The absence of the vacancy reduces possibility of formation of interfacial dislocations. In the line of this observation, no such interfacial dislocations have been observed in Figures 3.9, and 3.10. The interfacial energy can be estimated by Becker's model, which suggests the role of the concentration gradient across the interfaces. Interfacial energy is proportional to the square of the concentration gradient across the interface $\gamma \sim (\frac{dc}{dx})^2$. Interfacial surface energy can be express as $\gamma_{interface} = \gamma_{chemical} + \gamma_{structure}$. In the case of chessboard microstructure, $\gamma_{chemical} = 6a^2\gamma c$, $\gamma_{structure} = a^3.c\varepsilon.\gamma$, where c is elastic constant and ε is misfit strain and can be calculated by $\varepsilon = \frac{(a_c - a_t)}{(c_t - a_c)}$, here a_c = 8.3 Å, a_c = 8.1 Å and c_t = 8.8 Å. The atomic arrangement in the HR-phase contrast image shown in Figure 3.5b can be identified with the help of multislice image simulation. Figure 3.9 (b) illustrates simulated high-resolution phase-contrast image along $[\bar{1}12]$ zone axis. The Multislice image simulation has been done on JEMS software platform with Voltage = 200kV, C_s = 1.2 mm and Δf_{Sch}= -65.83 nm as operating conditions of the microscope. The image simulations were done by taking $CoFe_2O_4$ crystal information files as input parameters. The sample related parameters such as sample thickness and defocus value were chosen so that simulated images could match with the experimental image. After running lot of simulations with various combination of sample thickness and defocus values, the juxtaposition of simulated (surrounded by white rectangle) and experimental HR-phase contrast images reveal that most closely matched simulated images were generated at a sample thickness range (t) 10-20 nm with an interval 2.02 nm and depth of focus (D_{foc}) = 112 nm-113 nm with a focus step 0.3 nm (Figure 3.9 (b)).

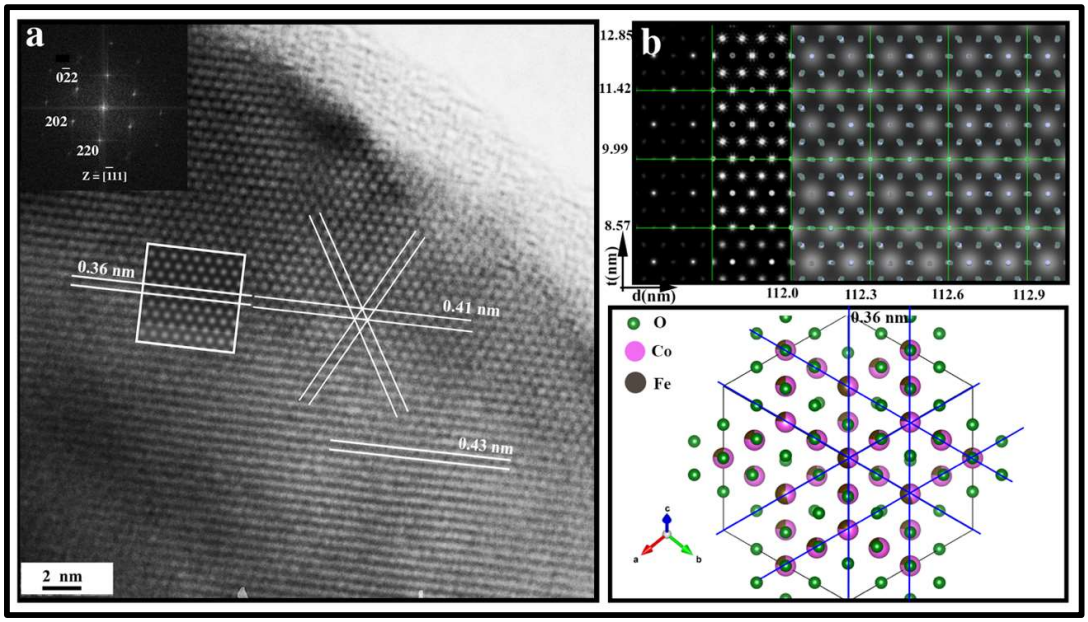

Figure 3.10: *(a) Phase contrast high-resolution image of* $Co_{0.6}Fe_{0.8}Mn_{1.6}O_{4+\delta}$ *(*$\delta<<1$*) along* $[\bar{1}12]$ *zone axis after heat treatment at 1250 ℃ for 24 hours followed by quenching in ice water and a subsequent aging at 375 ℃ for 150 hours. In the same image, simulated HR image is overlaid on experimental image (surrounded by solid white rectangle), (b) corresponding defocus-thickness map generated by multislice simulation method performed with voltage = 200kV,* C_s *= 1.2 mm and* Δf_{Sch}*= -65.83 nm. parameters used. (c) perspective view of unit cell of* $CoFe_2O_4$ *along* $[\bar{1}11]$.

The atomic projection on the simulated image showed that in the experimental image, $(1\bar{1}1)$ and (220) planes are imaged with d-spacings ~ 0.52 nm and ~ 0.31 nm. A similar observation has been made along $[\bar{1}11]$ zone axis (Figure 3.10), where alternative (220) planes is imaged with an atomic arrangement shown in Figure 3.10 (b).

3.4 Conclusions

The CoFeGaMnZn multicomponent oxide is observed to produce chessboard nanodomains after a long-term ageing treatment. The mechanism of chessboard nano domain formation is similar to that reported in ternary oxides in which multiple twinning-induced diffusive separation of ionic species takes place. The nanodomains in CoFeGaMnZn are significantly smaller than those seen in CoFeMn and ZnGaMn ternary oxides because the pseudo-spinodal segregation of ionic species is diffusion mediated, and this becomes slower with

an increase in the number of cationic species present. Minimization of strain energy and overall free energy in the multicomponent MCOs appear to be the driving forces behind systematic twinning in the spinel tetragonal *I* structure and the subsequent diffusive separation within this structure.

References

[1] J.W. Yeh, S.K. Chen, S.J. Lin, J.Y. Gan, T.S. Chin, T.T. Shun, C.H. Tsau, S.Y. Chang, Nanostructured high-entropy alloys with multiple principal elements: novel alloy design concepts and outcomes, Adv. Eng. Mater. 6 (2004) 299–303. https://doi.org/10.1002/adem.200300567.

[2] B. Cantor, I.T.H. Chang, P. Knight, A.J.B. Vincent, Microstructural development in equiatomic multicomponent alloys, Mater. Sci. Eng. A. 375–377 (2004) 213–218. https://doi.org/10.1016/j.msea.2003.10.257.

[3] B.S. Murty, J.W. Yeh, S. Ranganathan, High-Entropy Alloys, 2014.

[4] D.B. Miracle, O.N. Senkov, A critical review of high entropy alloys and related concepts, Acta Mater. 122 (2017) 448–511. https://doi.org/10.1016/j.actamat.2016.08.081.

[5] B.L. Musicó, D. Gilbert, T.Z. Ward, K. Page, E. George, J. Yan, D. Mandrus, V. Keppens, The emergent field of high entropy oxides: Design, prospects, challenges, and opportunities for tailoring material properties, APL Mater. 8 (2020) 0–16. https://doi.org/10.1063/5.0003149.

[6] W. Steurer, Single-phase high-entropy alloys – A critical update, Mater. Charact. 162 (2020) 110179. https://doi.org/10.1016/j.matchar.2020.110179.

[7] V. Shivam, J. Basu, R. Manna, N.K. Mukhopadhyay, Local composition migration induced microstructural evolution and mechanical properties of non-equiatomic $Fe_{40}Cr_{25}Ni_{15}$ $Al_{15}Co_5$ Medium-Entropy Alloy, Metall. Mater. Trans. A. 52 (2021) 1777–1789. https://doi.org/10.1007/s11661-021-06188-7.

[8] O.N. Senkov, J.D. Miller, D.B. Miracle, C. Woodward, Accelerated exploration of multi-principal element alloys with solid solution phases, Nat. Commun. 6 (2015) 6529. https://doi.org/10.1038/ncomms7529.

[9] Y. Ma, Y. Ma, Q. Wang, S. Schweidler, M. Botros, T. Fu, H. Hahn, T. Brezesinski, B. Breitung, High-entropy energy materials: Challenges and new opportunities, Energy Environ. Sci. 14 (2021) 2883–2905. https://doi.org/10.1039/d1ee00505g.

[10] A. Sarkar, L. Velasco, D. Wang, Q. Wang, G. Talasila, L. de Biasi, C. Kübel, T. Brezesinski, S.S. Bhattacharya, H. Hahn, B. Breitung, High entropy oxides for reversible energy storage, Nat. Commun. 9 (2018) 3400. https://doi.org/10.1038/s41467-018-05774-5.

[11] V.K. Pandey, Y. Shadangi, V. Shivam, J. Basu, K. Chattopadhyay, B. Majumdar,

B.N. Sarma, N.K. Mukhopadhyay, Synthesis, Characterization and thermal stability of nanocrystalline MgAlMnFeCu low-density high-entropy alloy, Trans. Indian Inst. Met. 74 (2021) 33–44. https://doi.org/10.1007/s12666-020-02114-4.

[12] V. Shivam, Y. Shadangi, J. Basu, N.K. Mukhopadhyay, Alloying behavior and thermal stability of mechanically alloyed nano AlCoCrFeNiTi high-entropy alloy, J. Mater. Res. 34 (2019) 787–795. https://doi.org/10.1557/jmr.2019.5.

[13] C.M. Rost, E. Sachet, T. Borman, A. Moballegh, E.C. Dickey, D. Hou, J.L. Jones, S. Curtarolo, J.P. Maria, Entropy-stabilized oxides, Nat. Commun. 6 (2015). https://doi.org/10.1038/ncomms9485.

[14] A. Sarkar, R. Djenadic, N.J. Usharani, K.P. Sanghvi, V.S.K. Chakravadhanula, A.S. Gandhi, H. Hahn, S.S. Bhattacharya, Nanocrystalline multicomponent entropy stabilised transition metal oxides, J. Eur. Ceram. Soc. 37 (2017) 747–754. https://doi.org/10.1016/j.jeurceramsoc.2016.09.018.

[15] R. Djenadic, A. Sarkar, O. Clemens, C. Loho, M. Botros, V.S.K. Chakravadhanula, C. Kübel, S.S. Bhattacharya, A.S. Gandhi, H. Hahn, Multicomponent equiatomic rare earth oxides, Mater. Res. Lett. 5 (2017) 102–109. https://doi.org/10.1080/21663831.2016.1220433.

[16] D. Bérardan, S. Franger, A.K. Meena, N. Dragoe, Room temperature lithium superionic conductivity in high entropy oxides, J. Mater. Chem. A. 4 (2016) 9536–9541. https://doi.org/10.1039/C6TA03249D.

[17] A. Sarkar, Q. Wang, A. Schiele, M.R. Chellali, S.S. Bhattacharya, D. Wang, T. Brezesinski, H. Hahn, L. Velasco, B. Breitung, High-entropy oxides: fundamental aspects and electrochemical properties, Adv. Mater. 31 (2019) 1806236. https://doi.org/10.1002/adma.201806236.

[18] C.L. Zhang, C.M. Tseng, C.H. Chen, S. Yeo, Y.J. Choi, S.-W. Cheong, Magnetic nanocheckerboards with tunable sizes in the Mn-doped $CoFe_2O_4$ spinel, Appl. Phys. Lett. 91 (2007) 233110. https://doi.org/10.1063/1.2821838.

[19] S. Park, Y. Horibe, T. Asada, L.S. Wielunski, N. Lee, P.L. Bonanno, S.M. O'Malley, A.A. Sirenko, A. Kazimirov, M. Tanimura, T. Gustafsson, S.-W. Cheong, Highly aligned epitaxial nanorods with a checkerboard Pattern in Oxide Films, Nano Lett. 8 (2008) 720–724. https://doi.org/10.1021/nl072848s.

[20] Y. Ni, A.G. Khachaturyan, From chessboard tweed to chessboard nanowire structure during pseudospinodal decomposition, Nat. Mater. 8 (2009) 410–414. https://doi.org/10.1038/nmat2431.

[21] C. Li, X. Han, F. Cheng, Y. Hu, C. Chen, J. Chen, Phase and composition controllable synthesis of cobalt manganese spinel nanoparticles towards efficient oxygen electrocatalysis, Nat. Commun. 6 (2015) 7345. https://doi.org/10.1038/ncomms8345.

[22] Z. S. Basinski, J.W. Christian, Crystallography of deformation by twin boundary movements in indium-thallium alloys, Acta Metall. 2 (1954) 101–116. https://doi.org/10.1016/0001-6160(54)90100-5.

[23] Z. Basinski, J. Christian, Interpenetrating "bands" in transformed indium-thallium alloys, Acta Metall. 4 (1956) 371–378. https://doi.org/10.1016/0001-6160(56)90026-8.

[24] D.Y. Cong, Y.D. Zhang, C. Esling, Y.D. Wang, J.S. Lecomte, X. Zhao, L. Zuo, Microstructural and crystallographic characteristics of interpenetrating and non-interpenetrating multiply twinned nanostructure in a Ni–Mn–Ga ferromagnetic shape memory alloy, Acta Mater. 59 (2011) 7070–7081. https://doi.org/10.1016/j.actamat.2011.07.062.

[25] J.W. Christian, S. Mahajan, Deformation twinning, Prog. Mater. Sci. 39 (1995) 1–157. https://doi.org/10.1016/0079-6425(94)00007-7.

[26] S. Praveen, J. Basu, S. Kashyap, R.S. Kottada, Exceptional resistance to grain growth in nanocrystalline CoCrFeNi high entropy alloy at high homologous temperatures, J. Alloys Compd. 662 (2016) 361–367. https://doi.org/10.1016/j.jallcom.2015.12.020.